The Astrophysical Journal, 846:113 (7pp), 2017 September 10 https://doi.org/10.3847/1538-4357/aa8363

Electromagnetic Structure and Electron Acceleration in Shock–Shock Interaction

Masaru Nakanotani[1,2], Shuichi Matsukiyo[3,4], Tohru Hada[3,4], and Christian X. Mazelle[2]
[1] Interdisciplinary Graduate School of Engineering Sciences, Kyushu University, 6-1 Kasuga-Koen, Kasuga, Fukuoka, 816-8580, Japan; nakanot@esst.kyushu-u.ac.jp
[2] IRAP, Université Paul Sabatier Toulouse III-CNRS, F-31028 Toulouse Cedex 4, France
[3] Faculty of Engineering Sciences, Kyushu University, 6-1 Kasuga-Koen, Kasuga, Fukuoka, 816-8580, Japan
Received 2016 June 20; revised 2017 July 12; accepted 2017 July 30; published 2017 September 7

Abstract

A shock–shock interaction is investigated by using a one-dimensional full particle-in-cell simulation. The simulation reproduces the collision of two symmetrical high Mach number quasi-perpendicular shocks. The basic structure of the shocks and ion dynamics is similar to that obtained by previous hybrid simulations. The new aspects obtained here are as follows. Electrons are already strongly accelerated before the two shocks collide through multiple reflection. The reflected electrons self-generate waves upstream between the two shocks before they collide. The waves far upstream are generated through the right-hand resonant instability with the anomalous Doppler effect. The waves generated near the shock are due to firehose instability and have much larger amplitudes than those due to the resonant instability. The high-energy electrons are efficiently scattered by the waves so that some of them gain large pitch angles. Those electrons can be easily reflected at the shock of the other side. The accelerated electrons form a power-law energy spectrum. Due to the accelerated electrons, the pressure of upstream electrons increases with time. This appears to cause the deceleration of the approaching shock speed. The accelerated electrons having sufficiently large Larmor radii are further accelerated through the similar mechanism working for ions when the two shocks are colliding.

Key words: acceleration of particles – instabilities – plasmas – shock waves

1. Introduction

Collisionless shocks have the potential for producing high-energy particles called cosmic rays. In the heliosphere energetic particles up to MeV energies are often observed in association with collisionless shocks like the terrestrial bow shock (e.g., Terasawa 1981), interplanetary (IP) shocks (e.g., Tsurutani & Lin 1985), and the heliospheric termination shock (Decker et al. 2008). Away from the heliosphere, supernova remnant shocks also generate high-energy cosmic rays (∼100 TeV) (Koyama et al. 1995). Furthermore, relativistic shocks in black hole jets (Dermer et al. 2009) or large-scale shocks in galaxy clusters (Kang et al. 1997) appear to produce ultra-high-energy cosmic rays above 1 EeV.

One of the most plausible acceleration mechanisms of cosmic rays is known as diffusive shock acceleration (DSA) (e.g., Blandford & Eichler 1987). Although most past studies assume the presence of a single shock, two shocks frequently come close to or even collide with each other in space. It was observed that IP shocks passed through the heliospheric termination shock (Gurnett et al. 2013). Multiple shock waves and their interactions are observed in a solar flare (Narukage et al. 2008). They also observed a radio burst around 100 ∼ 200 MHz emitted when one shock caught up with another. The collision of an IP shock and the bow shock was observed in situ by Hietala et al. (2011). Those authors reported ion acceleration in the shock–shock interaction by using multi-spacecraft data (*ACE*, *Wind*, *IMP-8*, *Geotail*, and *Interball-1*). They estimated that the seed particles already accelerated by the IP shock are further accelerated two to three times in their energy between the approaching two shocks. They interpreted that the acceleration is due to the first-order *Fermi* acceleration by the two shocks (two magnetic mirrors). A similar event was observed by Scholer & Ipavich (1983). Recently, a shock–shock interaction was also observed in a high-power laser experiment (Morita et al. 2013).

Various observational and experimental studies imply efficient particle acceleration or heating in a shock–shock interaction. However, detailed physics occurring in shock–shock interaction has not been understood. Self-consistent kinetic numerical simulation should provide useful insights. The only studies that used hybrid simulations were Cargill et al. (1986) and Cargill (1991). They found a dynamical change of magnetic field structure and acceleration of energetic ions when two supercritical (quasi-) perpendicular shocks collide. Cargill et al. (1986) demonstrated that the acceleration occurs due to multiple reflection of the ions when the distance between the two shocks becomes smaller than their Larmor radii.

A hybrid simulation treats ions as particles and electrons as a (massless) fluid. However, a detailed structure including the potential of the transition region of a shock is usually dependent on electron dynamics. Furthermore, electron acceleration in a multiple-shock system has not yet been investigated by using a self-consistent kinetic simulation. In this paper, we discuss a shock–shock interaction by using a 1D particle-in-cell (PIC) simulation. In particular, we focus on the electron acceleration process of two colliding shocks and the associated electromagnetic structures.

This paper is organized as follows. In Section 2, the simulation method and settings are described. An overview of the structures of colliding shocks are given in Section 3, mainly by comparing the fluid theory with the previous hybrid simulation. Ion and electron acceleration is discussed in Section 4. Section 5 focuses on the electron scale upstream waves and the associated wave–particle interactions. Section 6 provides a summary and discussions.

[4] International Center for Space Weather Science and Education, Kyushu University, 744 Motooka, Nishi-Ku, Fukuoka, 819-0395, Japan.

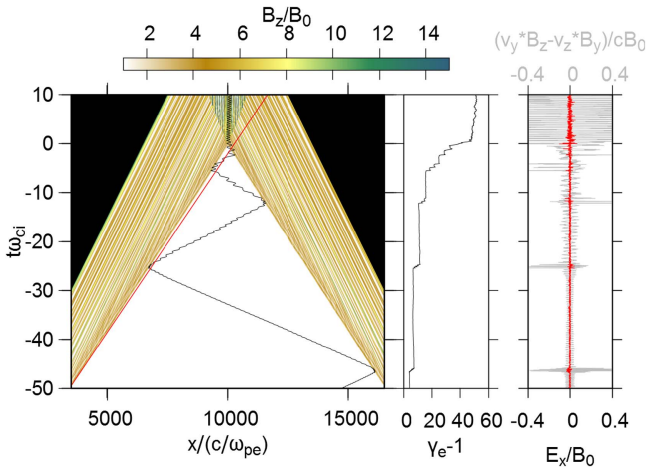

Figure 1. Space–time evolution of the z-component of magnetic field. The black region shows out of the walls and the white region is the upstream of the two shocks. An energetic electron trajectory is superimposed. The slope of the red line corresponds to the velocity of 0.136c. The time evolution of the energy (middle panel) and the electrostatic (red line) and magnetic (gray line) force experienced by the electron (right panel).

2. Method

Two colliding shocks are produced by using a 1D full PIC simulation. The code was originally developed and used in Matsukiyo et al. (2011) and Matsukiyo & Scholer (2012). For the present study, we changed the boundary conditions of the simulation code. Initially, we fill a homogeneous magnetized plasma at rest having a Maxwellian distribution function in a simulation system. Two boundaries initially at $x = 0$ and $x = 20000(c/\omega_{pe})$ are rigid walls at which particles and waves are specularly reflected. By moving the walls inward with constant speeds, two shocks are formed through the interaction between the background and the reflected plasmas. Hereafter, we refer the shock propagating from right (left) to left (right) as "Shock 1 (Shock 2)." Shock 1 and Shock 2 gradually approach each other and collide head-on. In this configuration, the simulation frame is the upstream rest frame before the two shocks collide. Because the speeds of the two walls are the same in magnitude here, the two shocks are essentially symmetric.

The background (or initial upstream) magnetic field is given as $\boldsymbol{B}_0 = B_0(\cos\theta_{Bn}, 0, \sin\theta_{Bn})$, where B_0 is the strength and θ_{Bn} is the shock angle defined as the angle between the magnetic field and the x-axis (shock normal). Here, we set $\theta_{Bn} = 60°$, the ratio of electron plasma to cyclotron frequencies $\omega_{pe}/\omega_{ce} = 10$, the ion and electron plasma beta $\beta_{i,e} = 0.5$, the ion to electron mass ratio $m_i/m_e = 100$, and the wall speed $v_w = \pm 0.1c$. Here, $\beta_{i,e} = 8\pi n_0 k_B T_{i,e}/B_0^2$, $\omega_{pe} = \sqrt{4\pi n_0 e^2/m_e}$ and $\omega_{ce} = eB_0/m_e c$, where e is the elementary charge, c is the speed of light, n_0 is the background ion and electron density, $T_{i,e}$ is the ion and electron temperature and k_B is the Boltzmann constant, respectively. The time resolution is $\Delta t = 0.05\omega_{pe}^{-1}$. The size of a spatial grid is $\Delta x = 0.05(c/\omega_{pe}) = \lambda_D$, where λ_D is the Debye length. The number of super particles per cell is 320. With these parameters, two symmetric shocks with Alfvén Mach number of 13.6 are produced.

3. Structures of Colliding Shocks

The color map in Figure 1 shows the space-time evolution of the z-component of the magnetic field. We define the time at the collision of the two shocks as $t\omega_{ci} = 0$, where $\omega_{ci} = eB_0/m_i c$.

Before the collision ($t\omega_{ci} < 0$), Alfvén Mach number of the two shocks is $M_A = 13.6$ and magnetosonic Mach number is $M_{ms} = 10.4$ so that the two shocks are supercritical (Kennel 1987). Snapshots in three phases (before, at, and after the collision) are plotted in Figure 2. Panels (a)–(c) show the profile of potential and magnetic field strength. In panels (d)–(f), the color scale denotes the phase space density of electrons, and the black line shows the density profile of electron. In panels (g)–(i), the color scale indicates show the phase space density of ions and the temperature of electrons and ions are denoted by the red and the black lines, respectively. The profiles of the two shocks roughly satisfy the Rankine–Hugoniot (RH) relation. From the density profile of electrons (the black line) in Figure 2(d), the downstream density averaged in $6000 \leqslant x/(c/\omega_{pe}) \leqslant 8100$ and $11{,}900 \leqslant x/(c/\omega_{pe}) \leqslant 14{,}000$ is indicated by the orange line which coincides with the value $3.9n_0$, estimated from the RH relation using $\Gamma = 5/3$ as polytrope index. The detailed downstream density profile denotes large amplitude fluctuations that are the characteristics of supercritical shocks (Quest 1986). We can see that there are energetic electrons between the two shocks (initial upstream thermal velocity is $v_{the} \sim 5v_A$) in the phase space of electron in Figure 2(d). The detailed acceleration mechanism of these electrons is discussed in the next section. On the other hand, we confirm that there are no energetic ions between the two shocks in Figure 2(g). As a result, the effective upstream temperature of electrons (the red line) is much higher than that of ions (the black line).

When the two shocks collide ($t\omega_{ci} = 0$), a strong peak of density can be seen (Figure 2(e)). The maximum density is about $10n_0$, which can be interpreted as the sum of the overshoots of the original two shocks. The width of the peak is about $35c/\omega_{pe} = 3.5c/\omega_{pi}$, where $\omega_{pi} = \sqrt{4\pi n_0 e^2/m_i}$. This value is almost the same as that obtained by the previous hybrid simulation with $M_A = 8$, $\beta = 1$, and $\theta_{Bn} = 90°$ (Cargill et al. 1986), although the direct comparison is difficult because of differences in parameters. Figure 2(b) shows the electrostatic potential with red line at $t\omega_{ci} = 0$ normalized to $m_i u_{sh}^2/2$, where u_{sh} is the shock speed in the upstream rest frame before the collision. The electrostatic potential steepens at the time of the collision the same as the density.

After the collision ($t\omega_{ci} > 0$), the two shocks propagate outward as seen in Figure 1. The speeds of the shocks are more or less constant corresponding to $M_A = 10.5$ and $M_{ms} = 2.3$, indicating that the two shocks are still supercritical. The black line in Figure 2(c) shows the profile of magnetic field strength; it is clear that magnetic fields are highly turbulent. The compression ratio of these shocks is about 2.2, which coincides with the value estimated from the RH relation assuming the polytropic index $\Gamma = 2$ in stead of $5/3$. This is because that after the collision, the shock angle becomes more perpendicular ($\theta_{Bn} \sim 82°$) so that the degrees of freedom of the system may be close to 2 (Gallant et al. 1992; Hoshino et al. 1992). The local increase (decrease) of the effective electron (ion) temperature downstream in $9600 < x/(c/\omega_{pe}) < 10400$ is seen in Figure 2(i), while the sum (the blue line) remains roughly constant. The temperatures are defined as $k_B T_j = \sum_i^N m_j(|\boldsymbol{v}_{ji} - \boldsymbol{u}_j|^2)/3N$. The subscript j indicates the particle species (ion and electron), the term i indicates the ith particle, and the parameter N is the number of particles. The vector $\boldsymbol{u}_j$ is an averaged velocity. The high electron temperature is the result of rapid electron acceleration just before the collision,

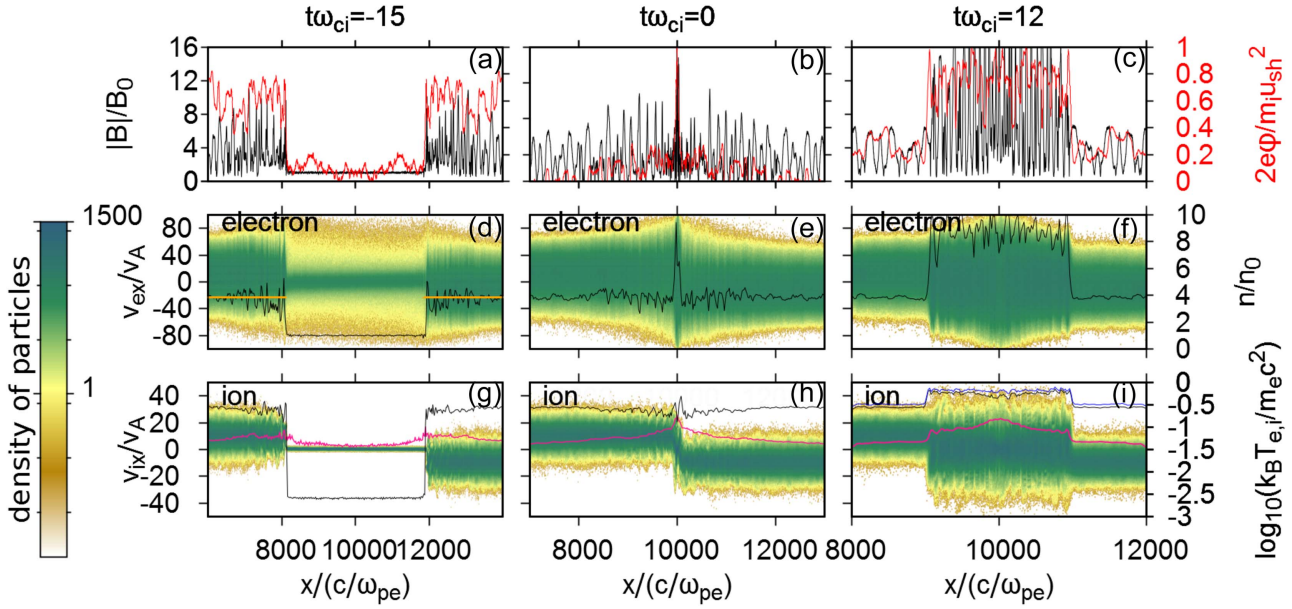

Figure 2. Profile of potential and magnetic field strength (a)–(c), phase space density of electrons (d)–(f), and ions (g)–(i) before, at, and after the collision from left to right, respectively. The black lines in the middle panels show the plasma density at the corresponding time. The black and red lines in the bottom panels show the ion and electron temperature, respectively, at the corresponding time. The blue line shows the sum of the electron and ion temperature. The orange lines correspond to 3.9.

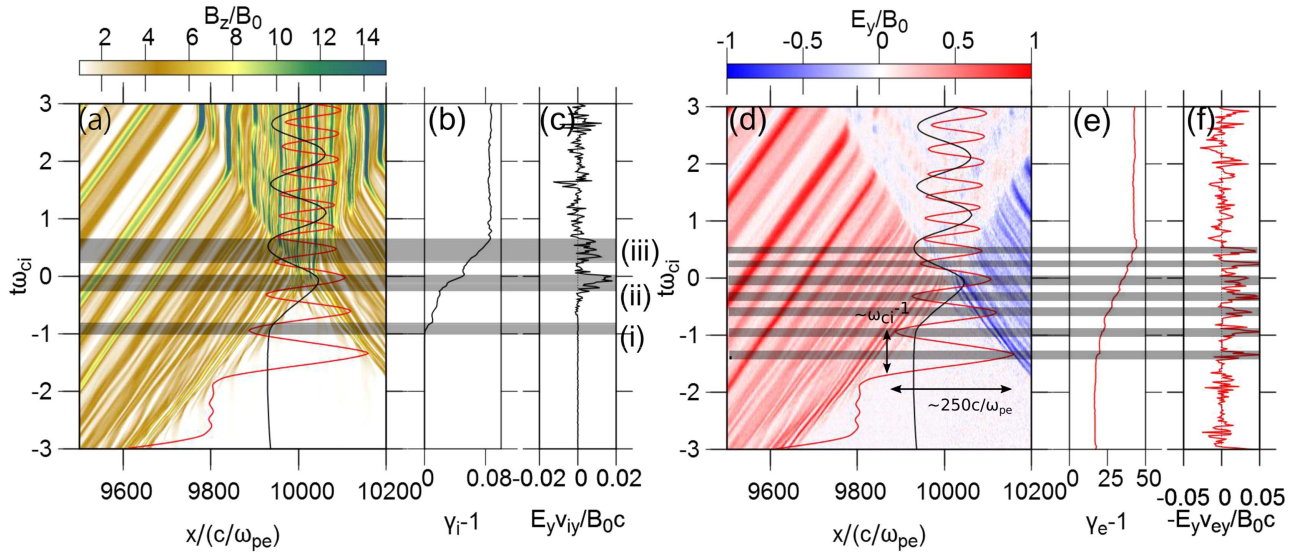

Figure 3. Accelerated ion trajectory (a) and (d), and time evolution of the energy (b) and $E_y v_{iy}$ (c) as displayed in black. An energetic electron trajectory (a) and (d) and time evolution of the energy (e) and $-E_y v_{ey}$ (f) around the colliding as displayed in red. Here, γ_e and γ_i are the Lorentz factors of the electron and the ion. The color map is the space-time evolution of B_z (a) and E_y (d).

which will be discussed in the following section. The electrons that accelerated rapidly just before the collision are tied to the local magnetic fields that are also amplified at the same time in the shock–shock collision and aligned almost perpendicular to x. The local increase of electron temperature is the remnant of these.

4. Particle Acceleration

Ions are accelerated through multiple interactions with the two shocks when their relative distance becomes shorter than the Larmor radii of the corresponding ions as discussed by Cargill et al. (1986). Figure 3 shows the trajectory of an accelerated ion (a) and (d) and the time evolution of the energy (b) and $E_y v_{iy}$ (c) with the black lines. The first acceleration occurs when the ion is reflected for the first time by the Shock 2 around $t\omega_{ci} \sim -1$ (the shaded region (i) in Figure 3). Next, the reflected ion penetrates the Shock 1 and is accelerated by the downstream motional electric field during $-0.25 \leqslant t\omega_{ci} \leqslant 0$ (the shaded region (ii) in Figure 3). During this second acceleration, the two shocks collide. Due to its gyro motion, the ion crosses two separating shocks and enters the upstream of the left-ward propagating shock. During its stay in the upstream region (the shaded region (iii) in Figure 3), the ion feels motional electric field upstream and is further accelerated. Here, one should note that the roles of upstream and downstream have changed after the collision. Therefore,

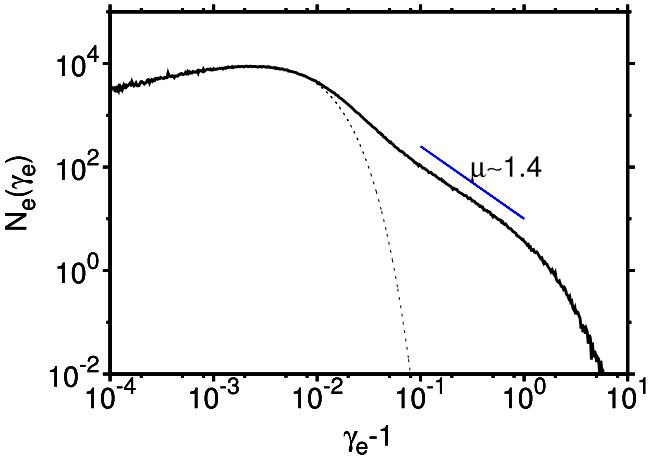

Figure 4. Solid line shows upstream electron energy distribution function at $t\omega_{ci} = -15$. The blue line with the index $\mu = 1.4$ is indicated as a reference. The dashed line shows the Maxwell distribution with the initial upstream condition.

the simulation frame has changed to the downstream rest frame. The total energy gain calculated in the simulation frame is about $10m_i v_{\rm sh}^2/2$, where $v_{\rm sh}$ is the speed of the shocks before the collision.

We have seen that there are energetic electrons between the two shocks before colliding (see Figure 2(d)). We find a non-thermal population that is initially absent. Figure 4 shows the energy spectrum of electrons upstream at $t\omega_{ci} = -15$ integrated from $8200c/\omega_{pe}$ to $11800c/\omega_{pe}$ (the black line). In comparison with the initial Maxwell distribution (the dashed line), a power-law tail is produced from 0.1 up to 1 in $\gamma - 1$, where γ is the Lorentz factor. The power-law index is about 1.4.

These non-thermal electrons are accelerated by being repeatedly reflected at the two shocks. In Figure 1, a high-energy electron trajectory on the space-time evolution of B_z is indicated by the black line, the middle panel is the time evolution of its energy. We find that the electron is accelerated when it interacts with the shocks until $t\omega_{ci} < 0$. We confirm that the magnetic force at the particle position is much larger than the electrostatic force (the right-most panel in Figure 1). This means that the reflections are mainly due to the magnetic mirror, and that the electrostatic potential is not important. At each reflection, the acceleration occurs through the shock drift acceleration (Leroy & Mangeney 1984; Wu 1984; Mann et al. 2009; Matsukiyo et al. 2011; Park et al. 2013). According to Park et al. (2013) and Mann et al. (2009), the energy increase of each reflection on the upstream rest frame is estimated as

$$\gamma_r = \gamma_i \left[1 + \frac{2u_t(u_{\rm sh}^{\rm HT} + v_{i||})}{c^2 - (u_{\rm sh}^{\rm HT})^2} \right], \quad (1)$$

where γ_r and γ_i are the Lorentz factor after and before a reflection, respectively, $u_{\rm sh}^{\rm HT} = u_{\rm sh}/\cos\theta_{Bn} > 0$ and $v_{i||}$ is parallel velocity before reflection. The speed $u_{\rm sh}$ and $u_{\rm sh}^{\rm HT}$ are the shock speed in the simulation frame and in the de Hoffmann–Teller frame. For the electron shown in Figure 1, the increments of the first two reflections are estimated as 1.85 and 1.65, respectively. Equation (1) gives $\gamma_r/\gamma_i = 1.69$ and 1.63 for the first two reflections by using the parallel velocity just before the reflection, $v_{i||} = 0.9c$ and $0.8c$, respectively. The values are in good agreement with the simulation result.

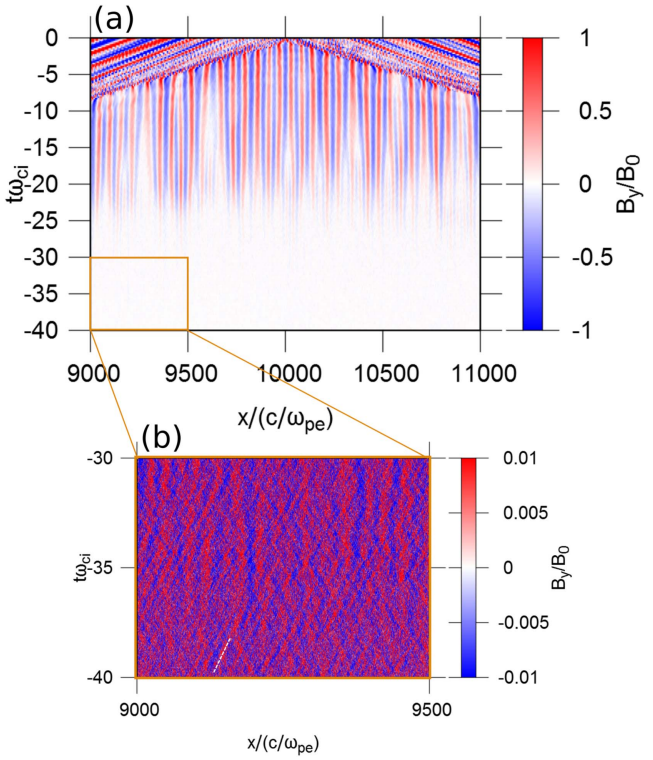

Figure 5. (a) Space–time evolution of the y component of the magnetic field and (b) the enlarged view with a different scale of By. The white dashed line corresponds to the speed of $0.02c$ is indicated as a reference.

At the collision ($t\omega_{ci} \sim 0$), pre-accelerated electrons are accelerated even more rapidly through the process different from the shock drift acceleration. Figures 3(d)–(f) also show a trajectory of such an electron with the red lines. At $t\omega_{ci} = -3$, the electron has been already pre-accelerated up to the Lorentz factor of $\gamma_e \sim 20$. Its gyro radius is $\rho_e \sim 125c/\omega_{pe}$ (indicated by the horizontal arrow) and its gyro period is $T_{e,\rm gyro}\omega_{ci} \sim 1$ (indicated by the vertical arrow). After $t\omega_{ci} > -1.5$, the electron gains energy in a multi-step manner when it glances off a downstream region of a shock. The acceleration time in each step, indicated by the gray bars, is clearly shorter than its gyro period. In each interaction with a shock, the electron is reflected after experiencing partial gyro motion in a downstream region. The direction of the partial gyro motion is always anti-parallel to the motional electric field, represented by the red and blue regions in Figure 3(d), so that $-E_y v_{ey} > 0$ as shown in Figure 3(f). This is actually what happens to the ion indicated by the black lines in Figures 3(a)–(c) and to the ions discussed by Cargill et al. (1986).

5. Wave Excitation and Its Role for Particle Acceleration

Figure 5(a) shows the space-time evolution of the y component of the magnetic field. The large amplitude waves (LAWs) are excited between the two shocks before the collision. The amplitude of these waves has spatial changes only. These changes appear nearly sinusoidal. In other words, these waves are non-propagating waves. They have a typical wavenumber of $k_w \sim 0.11\omega_{pe}/c$ and amplitude of $B_w \sim 0.5B_0$.

The excitation mechanism is the electron firehose instability due to an electron temperature anisotropy (Li & Habbal 2000). However, there is no anisotropy in the ion temperature because ions do not escape upstream in this particular case. The top

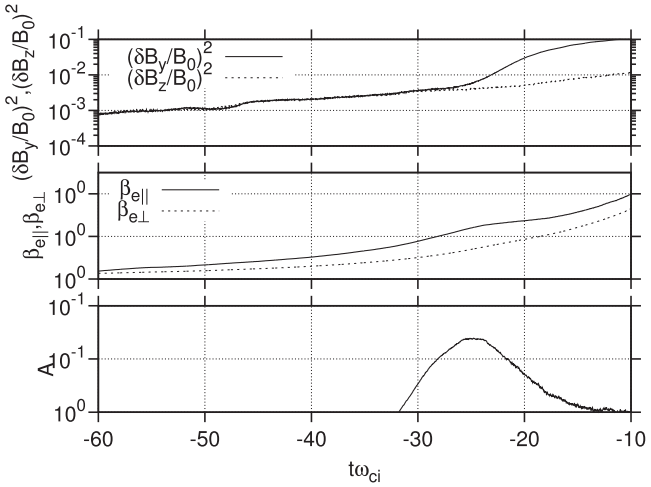

Figure 6. Time evolution of the increment of the y- (solid) and z- (dashed) component of the magnetic field fluctuations (top panel), the parallel (solid) and perpendicular (dashed) electron plasma beta (middle panel), and the criteria of the firehose instability (bottom panel).

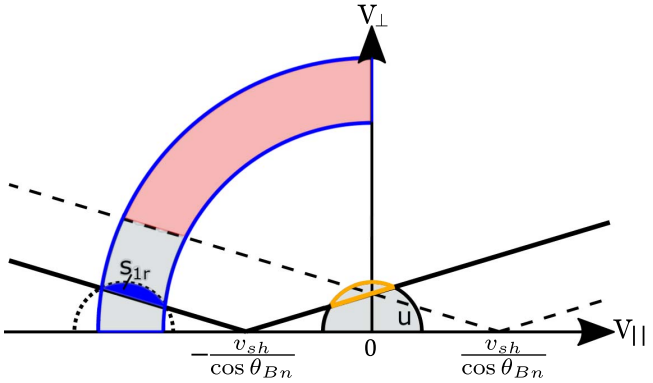

Figure 7. Schematic condition of the SDA in $v_{||}$–$v_\perp$ space on the upstream rest frame.

panel of Figure 6 shows the time evolution of magnetic fluctuations. The LAWs are visible in δB_y^2 (the solid line) from the time $t\omega_{ci} \sim -25$, the amplitude growth rate is about $0.18\omega_{ci}^{-1}$ at that time. The middle panel of Figure 6 shows the time evolution of the parallel (black line) and perpendicular (dashed line) electron beta ($\beta_{e\|}$, $\beta_{e\perp}$) averaged in the region between the two shocks. While both $\beta_{e\|}$ and $\beta_{e\perp}$ grow in time, $\beta_{e\|}$ is higher that $\beta_{e\perp}$, due to the reflected electrons that gain energy mostly parallel to the magnetic field through SDA (Matsukiyo et al. 2011). The bottom panel of Figure 6 shows the time evolution of the anisotropy factor defined as $A \equiv 1 - T_{e\perp}/T_{e\|} - S/\beta_{e\|}^{\alpha}$. According to Gary & Nishimura (2003), the firehose instability sets in when $A > 0$ for $S = 1.29$ and $\alpha = 0.97$. The values S and α are used here. When the LAWs start to grow, A is sufficiently large and after that A is decreased.

It is known that in the oblique firehose instability with $\theta > 30°$, where θ is the angle between $\boldsymbol{k}$ and $\boldsymbol{B}_0$, the waves become non-propagating and the fluctuating magnetic field excited is parallel to $\boldsymbol{k} \times \boldsymbol{B}_0$ (Li & Habbal 2000). Due to the dimensionality of the simulation, $\boldsymbol{k}$ directs the x direction. Therefore, only B_y is fluctuating, which is consistent with the above properties.

Before the excitation of the firehose instability, $-42.5 \leqslant t\omega_{ci} \leqslant -25$, the magnetic field fluctuations δB_y and δB_z gradually increase due to a resonant instability. In Figure 5 (b), one can identify the waves propagating with the phase speed of $\sim 2v_A$ (guided by the white dashed line) and wavelength of $\sim 20c/\omega_{pe}$. Evaluating $\zeta_n = (\omega - k_\| v_\| - n\omega_{ce})/\omega_{ce}$ for $n = 0, \pm 1, \pm 2$, we obtain $\zeta_0 \approx -0.91$, $\zeta_1 \approx -1.9$, $\zeta_{-1} \approx -0.089$, $\zeta_2 \approx -2.9$, and $\zeta_{-2} \approx 1.1$, respectively. This implies that the waves get excited via electron anomalous cyclotron resonance with $n = -1$. The waves are right-hand polarized. We estimate the growth rate of the instability from Figure 6 as $\sim 0.027\omega_{ci}$, which is in good agreement with the linear growth rate obtained by the kinetic dispersion relation.

The LAWs play a crucial role in the electron acceleration before the collision. Figure 7 schematically shows how some electrons are reflected and accelerated at the two shocks in the upstream plasma frame. Let us consider the electrons that initially distributed inside the semi-circle labeled by "u" (the shaded region). Suppose that the electrons first interact with the Shock 1. The two oblique solid lines denote the loss-cone of the Shock 1. Therefore, only the electrons outside the loss-cone bounded by the orange lines are reflected at the Shock 1. The reflected electrons are mapped to the blue region labeled "s_{1r}." The electrons are symmetrically reflected for the speed $-v_{sh}/\cos\theta_{Bn}$ as long as a shock speed and the speed of electrons (Park et al. 2013). As one can see, the electrons have smaller pitch angles after they are reflected. These electrons may not be able to be further reflected when they encounter-Shock 2 because they are inside the loss-cone, which is indicated by the two dashed lines. However, if the LAWs efficiently scatter these electrons in pitch angle, they may spread in the shaded area bounded by the two blue lines. After the scattering, Shock 2 may reflect the electrons outside the loss-cone (the red-shaded region).

To investigate the actual motion of electrons interacting with the LAWs, we use a test particle simulation in which we give the fields imitating the LAWs and the background magnetic field. In the test particle simulation, the back reaction of the particle dynamics is ignored; we solved a particle motion only in the given fields below:

$$\boldsymbol{B}/B_0 = \boldsymbol{b}_0 + \boldsymbol{b}_w, \boldsymbol{E} = 0, \tag{2}$$

$$\boldsymbol{b}_0 = (\cos\theta_{Bn}, 0, \sin\theta_{Bn}), \tag{3}$$

$$\boldsymbol{b}_w = (0, \kappa \sin kx, 0). \tag{4}$$

We solve the equations of motion of 4000 particles with the time step $\Delta t = 0.05\omega_{pe}^{-1}$ for $5\omega_{ci}^{-1}$ using the Buneman–Boris method. The LAWs are almost monochromatic waves approximated by $\boldsymbol{b}_w$ in Equation (4). As the initial condition, particles have various speeds ($0 < v < 0.99c$) and a constant pitch angle $\pi/6$. Furthermore, we define $\theta_{Bn} = 60°$, $\kappa = 0.5$, $k = 0.11(\omega_{pe}/c)$ from the simulation.

We find that energetic electrons are efficiently scattered in pitch angle between 0 and $\pi/2$. Figure 8(a) shows the particle distribution in the parallel and perpendicular velocity space at the end of the test particle simulation for $\kappa = 0.5$. The red and black points indicate particles in the phase space at the initial and the end of the simulation, respectively. Because there is no electric field in the test particle simulation, a particle moves along a circle whose radius remains constant with its initial speed in the phase space.

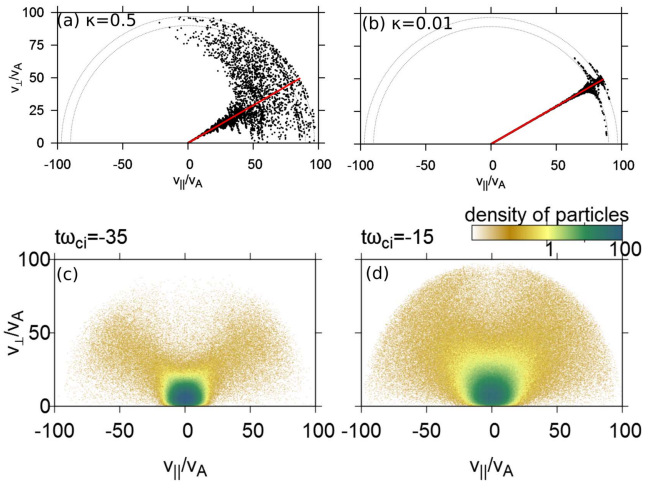

Figure 8. (a) and (b) are phase space of parallel and perpendicular velocity from the test particle simulation. The red and black points indicate the initial and final position of the particles for $\kappa = 0.5$ (a) and $\kappa = 0.01$ (b). The dashed curve corresponds with the speed of $0.9c$ and $0.97c$. Electron phase space density for parallel and perpendicular velocities between the two shocks from the PIC simulation at $t\omega_{ci} = -35$ before the LAWs are excited (c) and $t\omega_{ci} = -15$ after the excitation (d).

Such efficient scattering occurs through the cyclotron resonance. Now, the resonance condition is given as $k_{||}v_{||R} = n\omega_{ce}/\gamma_e$, where $k_{||} = k\cos\theta_{Bn}$, $v_{||R}$ is the particle speed parallel to $\boldsymbol{B}$, $\gamma_e = [1 - (v_{||R}^2 + v_{\perp R}^2)/c^2]^{-1/2}$ ($v_{\perp R}$ is the particle speed perpendicular to $\boldsymbol{B}_0$), and n is the harmonic number integer. We confirmed that efficient scattering occurs only for the particles satisfying the above resonance condition when the wave amplitude is small enough. Figure 8(b) shows the particle distribution in the parallel and perpendicular velocity space at the end of the test particle simulation for $\kappa = 0.01$. The other parameters are same with Figure 8(a). One can clearly see that two groups of particles are efficiently scattered in pitch angle. The particles with $v \sim 0.9c$ satisfy the resonance condition with $n = 1$ (the fundamental resonance), while the particles with $v \sim 0.97c$ satisfy the condition with $n = 2$ (the second harmonic resonance). Now, $\kappa = 0.5$ is rather large. Hence, a number of particles with wider velocity region can resonate with the LAWs and be scattered as in Figures 8(a) and (b). Because ions do not resonate with the LAWs (the resonance speed for ions, $v_{||R} \sim 0.02c$, is larger than the thermal speed of ions, $v_{\rm thi} = 0.005c$), they are not affected by those waves.

Figures 8(c) and (d) denote electron phase space density obtained from the PIC simulation at $t\omega_{ci} = -35$ and -15, respectively. Before that the LAWs are excited and the reflected electrons are distributed in relatively limited region in the phase space (Figure 8(c)). In contrast, after that the LAWs are excited, the reflected electrons are distributed in a wider region in phase space including large pitch angles (Figure 8(d)). This indicates that the electrons scattered by the LAWs and gaining large pitch angles can be easily reflected when they encounter the other shock. It should be also noted that some electrons have negative $v_{||}$. They have been scattered back by the LAWs toward the shock they first encountered. An example of such a trajectory is seen in the PIC simulation (the red line in Figure 3). This process is discussed by Matsukiyo et al. (2011) and Guo et al. (2014).

6. Summary and Discussions

In summary, we presented simulation results with respect to the head-on collision of two symmetric shocks by using a 1D full PIC simulation. The initial shock parameters are $M_{\rm A} = 13.6$, $\beta_{i,e} = 0.5$, $\theta_{Bn} = 60°$.

The simulation results are summarized as follows. Before the collision, some electrons are accelerated by repeatedly reflected at the two shocks. This acceleration is due to the shock drift acceleration. The maximum energy of the accelerated electrons is about 50 in Lorentz factor. Reflected electrons create a temperature anisotropy and excite LAWs through the electron firehose instability between the two shocks.

In colliding, ions are quickly accelerated by crossing the fronts of the two shocks a few times when the two shocks get close; the attainable energy is about $10m_i v_{\rm sh}^2/2$. The only electrons that are pre-accelerated before the colliding and have large a Larmor radius are also accelerated in the same way.

After the collision, the Mach number of the shocks decreases ($M_{\rm A} \sim 10.5$ and $M_{ms} \sim 2.3$), because the upstream Alfvén speed and fast magnetosonic speed for the new shocks quite increase. Because M_{ms} is rather small, the shock profile is nearly laminar.

Furthermore, we verified that the LAWs effectively scatter the reflected electrons in pitch angle. This effect promotes the successive reflection of the once reflected high-energy electrons.

For the specific parameters investigated here, only electrons are accelerated through the above mechanism. In spite of that some ions are specularly reflected at the same shocks, they return to the original shock due to their gyro motion, and they do not stream back toward upstream; this is due to the shock angle being too large (Gosling & Robson 1985). For smaller shock angles, it was reported that backstreaming ions are produced, some of which are accelerated through the process similar to that for electrons (Cargill 1991).

In the current simulation, any further electron and ion acceleration is not confirmed after $t\omega_{ci} = 1$. This may be due to the limited simulation time. After the collision, the upstream regions of the two shocks are highly turbulent. This is the preferred situation for the DSA process (e.g., Guo & Giacalone 2015). The shocks after the collision have rather small magnetosonic Mach numbers, as already mentioned in Section 3, and they are high beta quasi-perpendicular shocks. It is pointed out that the shocks of this type can efficiently accelerate electrons through the relativistic shock drift acceleration mechanism (Matsukiyo et al. 2011).

We observe the speed of the two shocks are clearly modified later in the simulation ($t\omega_{ci} \geqslant -10$). One possible reason for this is that the propagation for the shocks has been free from the influence due to the two spatial boundaries after $t\omega_{ci} \sim -10$. Another possibility is nonlinear modification of the shock speed due to the effect of the pre-accelerated electrons already before the shocks collide. In Figure 1, the blue line is the tangent to the shock front during the time $-65 \leqslant t\omega_{ci} \leqslant -45$. Here, $t\omega_{ci} = -45$ corresponds to the time at which the reflected electrons first reach the other shocks. The slope of the blue line indicates the initial shock speed, which is $13.6V_{\rm A}$. One can see that the gap between the blue line and the shock front position becomes clear in the later time ($t\omega_{ci} > -10$). The shock speed decreases from initial $13.6V_{\rm A}$ to $12.9V_{\rm A}$ just before the collision. This is interpreted as the modification of the shock (Drury & Voelk 1981), probably

because of the large electron pressure provided by the reflected high-energy electrons (Figure 2). The modification is too small to apparently change the compression ratio. We expect that it becomes clearer if a sufficiently large-scale simulation is carried out.

We thank B. Lembège for valuable discussions. The numerical simulations were performed on the Fujitsu PRIMERGY CX400 at Kyushu University. M.N. is supported by "Boursier du Gouvernement Français." S.M. is supported by a Grant-in-Aid for Scientific Research (C) 25400479 from JSPS. We are also grateful to ISSI (Bern) for their support of the team "Physics of the injection of particle acceleration at astrophysical, heliospheric, and laboratory collisionless shocks."

References

Blandford, R., & Eichler, D. 1987, PhR, 154, 1
Cargill, P. J. 1991, ApJ, 376, 771
Cargill, P. J., Goodrich, C. C., & Papadopoulos, K. 1986, PhRvL, 56, 1988
Decker, R. B., Krimigis, S. M., Roelof, E. C., et al. 2008, Natur, 454, 67
Dermer, C. D., Razzaque, S., Finke, J. D., & Atoyan, A. 2009, NJPh, 11, 065016
Drury, L. O., & Voelk, J. H. 1981, ApJ, 248, 344
Gallant, Y. A., Hoshino, M., Langdon, A. B., Arons, J., & Max, C. E. 1992, ApJ, 391, 73
Gary, S. P., & Nishimura, K. 2003, PhPl, 10, 3571
Gosling, J. T., & Robson, A. E. 1985, GMS, 35, 141
Guo, F., & Giacalone, J. 2015, ApJ, 802, 97
Guo, X., Sironi, L., & Narayan, R. 2014, ApJ, 797, 47
Gurnett, D. A., Kurth, W. S., Burlaga, L. F., & Ness, N. F. 2013, Sci, 341, 1489
Hietala, H., Agueda, N., Andréeová, K., et al. 2011, JGRA, 116, A10105
Hoshino, M., Arons, J., Gallant, Y. A., & Langdon, A. B. 1992, ApJ, 390, 454
Kang, H., Rachen, J. P., & Biermann, P. L. 1997, MNRAS, 286, 257
Kennel, C. F. 1987, JGR, 92, 13427
Koyama, K., Petre, R., Gotthelf, E. V., et al. 1995, Natur, 378, 255
Leroy, M. M., & Mangeney, A. 1984, AnGeo, 2, 449
Li, X., & Habbal, S. R. 2000, JGR, 105, 27377
Mann, G., Warmuth, A., & Aurass, H. 2009, A&A, 494, 669
Matsukiyo, S., Ohira, Y., Yamazaki, R., & Umeda, T. 2011, ApJ, 742, 47
Matsukiyo, S., & Scholer, M. 2012, JGRA, 117, A11105
Morita, T., Sakawa, Y., Kuramitsu, Y., et al. 2013, HEDP, 9, 187
Narukage, N., Ishii, T. T., Nagata, S., et al. 2008, ApJL, 684, L45
Park, J., Ren, C., Workman, J. C., & Blackman, E. G. 2013, ApJ, 765, 147
Quest, K. B. 1986, JGR, 91, 8805
Scholer, M., & Ipavich, F. M. 1983, JGR, 88, 5715
Terasawa, T. 1981, JGR, 86, 7595
Tsurutani, B. T., & Lin, R. P. 1985, JGR, 90, 1
Wu, C. S. 1984, JGR, 89, 8857